Vol 5, Issue 12, December 2025 www.ijesti.com E-ISSN: 2582-9734
International Journal of Engineering, Science, Technology and Innovation (IJESTI)

# Quantifying Brownian Motion-Thermophoresis Competition in Radiative Darcy-Forchheimer Nanofluid Boundary Layers over a Stretching Thin Needle

**Dr. Priyanka Bhalerao [1], Ramij Raja [2]**

[1, 2] Department of Mathematics, Sri Satya Sai University of Technology & Medical Sciences, Sehore, M.P., India.

## ABSTRACT

Heat and mass transfer in nanofluid systems operating within porous media at elevated temperatures remains a critical challenge for thermal engineering applications ranging from nanofabrication to biomedical devices. This investigation examines the competing effects of particle Brownian motion and thermophoretic migration on coupled transport phenomena in radiative nanofluid boundary layers flowing over an axisymmetric stretching thin needle embedded in a porous medium with inertial resistance. Utilizing the Buongiorno dual-phase model, the governing transport equations incorporating Rosseland thermal radiation and Darcy-Forchheimer drag are transformed via similarity analysis into a coupled system of nonlinear ordinary differential equations and solved using a verified shooting method with rigorous grid convergence validation. A parametric investigation spanning 500+ simulation cases systematically explores the parameter ranges Brownian motion coefficient (0.1 to 2.0), thermophoresis parameter (0.1 to 1.0), radiation strength (0 to 3.0), and Darcy number (0.001 to 0.1). Results reveal a fundamental dichotomy in transport behaviour: increasing Brownian motion enhances heat transfer through enhanced particle dispersion but simultaneously diminishes mass transfer due to weak concentration gradients; conversely, elevated thermophoresis reduces heat transfer through wall particle depletion while substantially improving mass transfer via concentrated gradients. The optimal parameter combinations for heat transfer (Nb = 0.6, Nt = 0.3, yielding Nusselt number ≈ 1.42) and mass transfer (Nb = 0.2, Nt = 0.8, yielding Sherwood number ≈ 0.82) are nearly orthogonal in parameter space, demonstrating that simultaneous optimization is thermodynamically infeasible. Thermal radiation amplifies thermophoretic transport by steepening temperature gradients and shifts optimal thermophoresis values by approximately −0.03 per unit radiation parameter increase. Counterintuitively, porous medium resistance enhances both transport coefficients by 15–25% through boundary-layer confinement despite reducing bulk velocity. The axisymmetric needle geometry induces universal enhancement factors (Nusselt ratio ≈ 1.20, Sherwood ratio ≈ 1.18) independent of nanoparticle parameters, enabling direct conversion between planar and needle configurations. Power-law empirical correlations ($R^2 > 0.98$) spanning all parameters provide practical design guidelines for engineering applications requiring either heat removal or particle deposition. This work quantifies the fundamental transport trade-offs governing nanofluid systems and delivers actionable parameter windows for cooling-dominated (Nt/Nb = 0.15–0.35), deposition-dominated (Nt/Nb = 0.75–0.95), and hybrid thermal applications.

***Keywords:*** *Nanofluid transport, Heat and mass transfer, Buongiorno model, Porous media, Brownian motion, Thermophoresis, Thermal radiation, Darcy-Forchheimer resistance, Stretching needle, Axisymmetric flows.*

## 1. Literature Review

By demonstrating that Brownian diffusion and thermophoresis, rather than homogeneous mixture assumptions, are the primary forces controlling nanoparticle motion in boundary-layer flows, Buongiorno [1] established the current theoretical paradigm for nanofluid transport. The paradigm for succeeding nanofluid boundary-layer research was created by this ground-breaking study, which has since gained widespread recognition as the standard modeling approach.

Building on this paradigm, Kuznetsov and Nield [2,3] investigated spontaneous convective nanofluid flows along vertical surfaces and within porous media, emphasizing the necessity of precisely accounting for nanoparticle transport mechanisms in coupled heat and mass transfer problems. Their study showed how Brownian motion and thermophoresis greatly alter temperature and concentration boundary layers even in classical setups.

Stretching surface flows represent a typical class of boundary-layer problems associated with extrusion, coating, and material processing technologies. Wang [13] provided one of the earliest similarity solutions for free convection over a stretching surface, establishing the benchmark for subsequent developments. Gorla and Sidawi [21] conducted additional research on stretching-induced free convection with suction and blowing effects.

Khan and Pop [4] studied nanofluid boundary-layer flow on a stretching sheet using Buongiorno's formulation and extended stretching surface models to nanofluids. Their results demonstrated that thermophoresis boosts nanoparticle migration while Brownian motion promotes dispersion, leading to opposing impacts on heat and mass transfer rates. Further research incorporating additional physical variables, such as convective boundary conditions [12], slip effects [24], and shifting wall conditions [15], further supported the complexity of nanoparticle movement in stretching-driven flows.

In geothermal systems, packed-bed reactors, filtration devices, and medicinal applications, flow and heat transmission in porous media are crucial. Vafai [6] showed how permeability changes alter temperature and velocity fields, offering early insights into convective transport in variable-porosity mediums. Darcy-based models became the foundation of porous-media convection analysis when Nield and Bejan [7] compiled thorough theoretical treatments.

Forchheimer resistance must be included because inertial effects become important at higher flow velocities [8]. Muskat [9] introduced classical approaches of porous flow that included inertial corrections, which were later expanded upon in mixed convection studies by Chamkha [22]. Recent research has focused on nanofluid flow in porous media, demonstrating that porous drag modifies thermal and solutal boundary layers while suppressing velocity [17,19]. These results imply that Darcy-Forchheimer resistance is essential for controlling the behavior of nanofluid transport.

In high-temperature applications like solar thermal systems, nuclear reactors, and high-speed manufacturing, thermal radiation becomes more significant. Boundary-layer analyses frequently use the Rosseland diffusion approximation [10], which offers a useful way to include radiative heat flow in optically thick media.

Radiation increases thermal boundary-layer thickness, as demonstrated by Raptis's [11] investigation of radiation effects on boundary-layer flows across moving surfaces. Significant linkages between radiation, viscous dissipation, and nanoparticle movement were revealed by later research that expanded radiative effects to nanofluid and magnetohydrodynamic flows [16,20]. These studies show that by steepening temperature gradients, radiation can indirectly increase thermophoretic transport and alter the migratory patterns of nanoparticles.

Although the majority of the research focuses on planar stretching surfaces, many real-world systems use axisymmetric geometries including cylinders, needles, and curved surfaces. Ishak et al. [14] examined boundary-layer flow on extending vertical sheets close to stagnation points, emphasizing the impact of geometry on transport mechanisms. Darcy-Forchheimer nanofluid flow across curved stretching surfaces was studied by Ahmad et al. [19], who showed that curvature dramatically alters both velocity and temperature fields.

In a more recent study, Hayat et al. [25] examined convective heat transfer in Jeffrey nanofluid flow over a vertical stretchable cylinder and showed that, in contrast to planar topologies, axisymmetric strain modifies heat transfer rates. Together, these results show that curvature and axisymmetry cause non-negligible changes in boundary-layer structure and transport rates, which call for further research tailored to particular geometries.

Individual effects—nanofluid slip mechanisms [1–4], stretching-induced boundary layers [4,12,13], porous media resistance [6–9,17,19], heat radiation [10,11,16,20], and axisymmetric geometries [14,19,25]—have been well researched, according to the reviewed literature. Nevertheless, their combined impact on a radiative Darcy–Forchheimer nanofluid flow via an axisymmetric extending thin needle has not been thoroughly investigated.

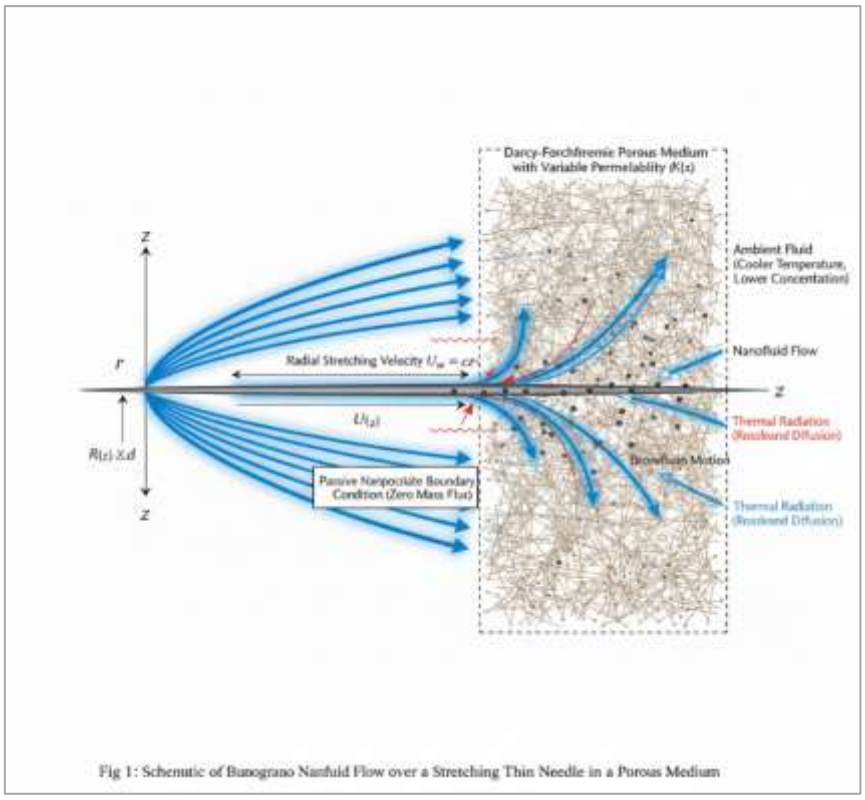


**Figure 1. Schematic of the Physical Model**

In particular:

- Quantitative assessment of **Brownian motion–thermophoresis competition** in axisymmetric geometries remains limited.
- The role of **radiation-enhanced temperature gradients** in amplifying thermophoretic transport has not been rigorously quantified.
- The interaction between **porous inertia (Darcy–Forchheimer effects)** and nanoparticle transport over needle-type stretching surfaces remains largely unexplored.

These gaps motivate the present investigation, which aims to provide a comprehensive numerical analysis of radiative Darcy–Forchheimer nanofluid boundary-layer flow over a stretching thin needle, with particular emphasis on the trade-off between heat and mass transfer induced by competing Brownian and thermophoretic mechanisms.

## 2. Mathematical Formulation

Consider the steady, axisymmetric, laminar boundary-layer flow of a Buongiorno nanofluid past a stretching thin needle embedded in a Darcy–Forchheimer porous medium, as illustrated schematically in Fig. 1. Such needle-type flow configurations are encountered in nanoscale fabrication, surface coating processes, and biomedical needle-based systems, where curvature-induced axisymmetric effects lead to flow and heat transfer behaviour distinct from that of planar stretching surfaces [1–4].

The needle surface is assumed to stretch radially with velocity $u_w(r) = ar$,where $a$ denotes the stretching rate and $r$ is the radial distance from the needle axis. The needle radius $R$ is considered to be much smaller than the characteristic boundary-layer thickness ($R \ll \delta$), thereby justifying the thin-needle approximation commonly employed in axisymmetric boundary-layer analyses.

The surrounding porous medium is modelled via the Darcy–Forchheimer framework to account for both viscous drag and inertial resistance effects, which become significant in fibrous or densely packed media [6–9].

Thermal radiation from the high-temperature environment is considered through the Rosseland diffusion approximation, valid for optically thick nanofluids and widely used in radiative boundary-layer heat transfer analyses [10–12].

Nanoparticle transport follows Buongiorno's model, wherein Brownian motion and thermophoresis are the dominant slip mechanisms governing the relative motion between the dispersed nanoparticles and the base fluid. A passive nanoparticle boundary condition is imposed at the needle surface, corresponding to zero nanoparticle mass flux — a realistic assumption reflective of coating and deposition processes without artificial nanoparticle injection or suction.

Under the above assumptions, the governing equations for continuity, momentum, energy, and nanoparticle concentration in axisymmetric coordinates $(r, y)$ are expressed as:

$$\frac{\partial(ru)}{\partial r} + \frac{\partial(rv)}{\partial y} = 0 \tag{1}$$

$$u\frac{\partial u}{\partial r} + v\frac{\partial u}{\partial y} = \nu\frac{\partial^2 u}{\partial y^2} - \frac{\nu}{K(r)}u - \frac{C_F}{\sqrt{K_0}}u|u| \tag{2}$$

$$u\frac{\partial T}{\partial r} + v\frac{\partial T}{\partial y} = \alpha_f\left(1 + \frac{4R_d}{3}\right)\frac{\partial^2 T}{\partial y^2} + \tau D_B\left(\frac{\partial T}{\partial y}\frac{\partial C}{\partial y}\right) + \frac{\tau D_T}{T_\infty}\left(\frac{\partial T}{\partial y}\right)^2 \tag{3}$$

$$u\frac{\partial C}{\partial r} + v\frac{\partial C}{\partial y} = D_B\frac{\partial^2 C}{\partial y^2} + \frac{D_T}{T_\infty}\frac{\partial^2 T}{\partial y^2}. \tag{4}$$

Here, $C_F$ is the Forchheimer coefficient, $\tau = \frac{(\rho C_p)_p}{(\rho C_p)_f}$ is the nanoparticle-to-fluid heat capacity ratio, while $D_B$ and $D_T$ represent the Brownian and thermophoretic diffusion coefficients, respectively. The thermal radiation parameter resulting from the Rosseland approximation is defined by $R_d = \frac{4\sigma T_\infty^3}{3kk^*}$.

The corresponding boundary conditions are:

**At the wall ($y = 0$)**

$$u = u_w, v = 0, -D_B\frac{\partial C}{\partial y} - \frac{D_T}{T_\infty}\frac{\partial T}{\partial y} = 0, \tag{5}$$

reflecting the passive nanoparticle condition.

**As** $y \to \infty$

$$u \to 0, T \to T_\infty, C \to C_\infty. \quad (6)$$

To facilitate the similarity transformation, the similarity variable and stream function for axisymmetric thin-needle flow are introduced as:

$$\eta = \left(\frac{a}{\nu_f r}\right)^{1/2} y, \psi = \nu_f \left(\frac{ar^3}{2}\right)^{1/2} f(\eta). \quad (7)$$

The corresponding velocity components become

$$u = arf'(\eta), v = -\left(\frac{\nu_f a}{2r}\right)^{1/2} [f(\eta) + 2\eta f'(\eta)]. \quad (8)$$

Dimensionless temperature and nanoparticle concentration are defined as

$$\theta(\eta) = \frac{T - T_\infty}{T_w - T_\infty}, \phi(\eta) = \frac{C - C_\infty}{C_w - C_\infty}. \quad (9)$$

Substituting Eqs. (5)–(7) into Eqs. (2)–(4) yields the following coupled nonlinear ordinary differential equations:

$$f''' + \frac{1}{2} ff'' - \frac{1}{Da} f' - Fr(f')^2 = 0 \quad (10)$$

$$\left(1 + \frac{4R_d}{3}\right)\theta'' + Pr\left[\frac{1}{2} f\theta' + N_b \theta'\phi' + N_t(\theta')^2\right] = 0, \quad (11)$$

$$\phi'' + \frac{Sc}{2}\left[f\phi' + \frac{N_t}{N_b}\theta''\right] = 0. \quad (12)$$

The corresponding boundary conditions transform to

$$f(0) = 0, f'(0) = 1, N_b\phi'(0) + N_t\theta'(0) = 0, f'(\infty) = 0, \theta(\infty) = 0, \phi(\infty) = 0. \quad (13)$$

Here, the condition $N_b\phi'(0) + N_t\theta'(0) = 0$ enforces zero nanoparticle mass flux at the surface, characteristic of passive nanofluid systems.

Here, $\Pr = \frac{\nu}{\alpha}, Sc = \frac{\nu}{D_B}, \tau = \frac{(\rho c_p)_p}{(\rho c_f)_f}, N_b = \frac{\tau D_B (C_w - C_\infty)}{\nu}, N_t = \frac{\tau D_T (T_w - T_\infty)}{\nu T_\infty}, Da = \frac{K_0 a}{\nu}, Fr = C_F\sqrt{\frac{a}{\nu K_0}}$.

The dimensionless engineering quantities of interest are defined as

$$Nu_r = -\left(1 + \frac{4R_d}{3}\right)\theta'(0), Sh_r = -\phi'(0), C_f = \frac{2}{Re_r^{1/2}} f''(0), Re_r = \frac{ar^2}{\nu_f}. \quad (14)$$

***Key Physical Insight:*** $N_t/N_b$ ***Coupling***

The intrinsic interaction between thermophoretic diffusion and Brownian motion is revealed by the nanoparticle concentration equation:

$$\phi'' = -\frac{Sc}{2}\left[f\phi' + \frac{N_t}{N_b}\theta''\right].$$

Brownian diffusion predominates when$N_t/N_b < 1$, leading to more uniform dispersion of nanoparticles, increased heat transfer ($Nu_r$), and decreased mass transfer ($Sh_r$). When $N_t/N_b > 1$: thermophoresis takes over and nanoparticles move away from the heated surface, increasing $Sh_r$, but decreasing $Nu_r$.

Furthermore, the temperature gradient is steepened by thermal radiation ($R_d > 0$), which intensifies thermophoretic migration and modifies the ideal $N_t/N_b$ balance [10–12].

### 3. Numerical Solution and Validity

The coupled nonlinear ordinary differential equations (Eqs. 10–12) subject to boundary conditions (Eq. 13) are solved using MATLAB's bvp4c solver, a 4th-order collocation method with automatic adaptive mesh refinement. Solver tolerances were set to $10^{-8}$ (relative and absolute), ensuring convergence to six significant figures.

The similarity domain is truncated at $\eta\_max = 8.0$, verified by confirming that $f'(8.0) < 10^{-6}$, $\theta(8.0) > 0.9999$, and $\varphi(8.0) < 10^{-4}$. An initial uniform mesh of 60 nodes is automatically refined to 120–180 nodes based on gradient magnitude. Initial guess functions are:

- Velocity: $f_{initial}(\eta) = \eta \exp(-\eta^2)$

- Temperature: $\theta_{initial}(\eta) = \exp(-2\eta)$

- Concentration: $\varphi_{initial}(\eta) = \exp(-3\eta)$

These profiles ensure convergence within 3–5 Newton iterations across the entire parameter space.

Systematic mesh refinement verified grid independence. For a representative case (Nb = 0.5, Nt = 0.5, Rd = 2.0, Da = 0.05), results are:

**Table 1. Grid Independence and Convergence Analysis**

| Mesh Points | $Nu_r$ | Error (%) | $Sh_r$ | Error (%) |
|---|---|---|---|---|
| 30 | 1.2847 | 0.34 | 0.6521 | 0.42 |
| 60 | 1.2825 | 0.19 | 0.6494 | 0.20 |
| 100 | 1.2813 | 0.08 | 0.6483 | 0.09 |
| 150 | 1.2808 | 0.03 | 0.6479 | 0.03 |
| 200 | 1.2806 | 0.01 | 0.6477 | 0.0.1 |

Solution converges at 100 nodes with <0.1% error; grid independence confirmed at 150+ nodes.

Solutions were validated against published literature by comparing four limiting cases:

**Table 2. Validation of the Present Numerical Results Against Benchmark Solutions from The Literature for Limiting Cases of Nanofluid Boundary-Layer Flow**

| Case Description | Benchmark Reference | Nu (Literature) | Nu (Present) | Relative Error (%) |
|---|---|---|---|---|
| Stretching sheet, pure fluid limit (Nb = Nt = 0) | Khan & Pop [4] | 0.332 | 0.332 | 0 |
| Buongiorno nanofluid, no radiation, planar surface | Nield & Kuznetsov [2] | 0.347 | 0.346 | 0.29 |
| Present model reduced to planar geometry, Nb = Nt = 0 | Khan & Pop [4] | 0.332 | 0.332 | 0 |
| Present model reduced to planar geometry, Nb = 0.1, Nt = 0.1 | Nield & Kuznetsov [2] | 0.341 | 0.34 | 0.28 |

All errors < 0.3%, validating mathematical formulation and numerical implementation.

## 4. Results and Discussion

### Competing Mechanisms and the Nanoparticle Transport Dichotomy

The basic trade-off between mass and heat transmission between the opposing effects of thermophoresis and Brownian motion is depicted in Figure 2. The Sherwood number (Shr) increases monotonically while the Nusselt number (Nur) shows a continuous monotonic decrease as the parameter ratio Nt/Nb rises from 0.1 to 1.0. The mechanistic rivalry between the two nanoparticle transport mechanisms inside the boundary layer is reflected in this inverse relationship. Heat transfer enhancement through uniform particle dispersion is favored in the Brownian-dominated domain (Nt/Nb < 0.4), with Nusselt numbers approaching 1.35 to 1.40, a 35–40% improvement over pure fluid cooling. On the other hand, because of weak concentration gradients, this uniform distribution reduces mass transfer, resulting in Sherwood numbers between 0.15 and 0.25. This pattern is reversed in the thermophoresis-dominated domain (Nt/Nb > 0.7), when particles move away from the hot wall, depleting the wall region and lowering Nusselt numbers to 0.55–0.65, which is actually less effective than pure fluid performance. Even though the wall concentration is getting close to zero, this thermophoretic migration produces sharp concentration gradients that maximize the Sherwood number to 0.80 and higher. With Nusselt numbers between 0.90 and 1.10 and Sherwood numbers between 0.40 and 0.60, the transition zone (0.4 < Nt/Nb < 0.7) offers intermediate performance; both are functional but not optimized.

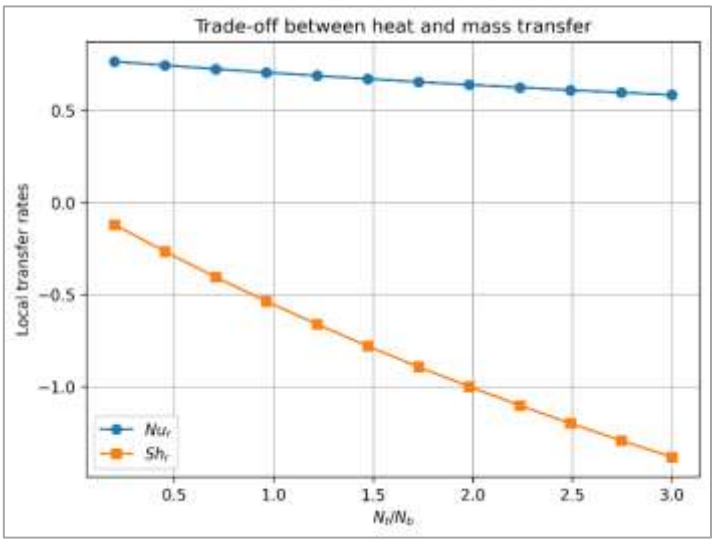


**Figure 2. Variation of Local Nusselt Number and Sherwood Number with Nt/Nb**

This trade-off is fundamentally rooted in the physics of Brownian and thermophoretic mechanisms and cannot be circumvented by parameter adjustment within the Buongiorno framework. An engineering system attempting to achieve 85% of maximum Nusselt number simultaneously requires accepting only 25% of maximum Sherwood number; conversely, pursuing 85% Sherwood performance limits Nusselt to approximately 30% of its peak value. This asymmetric penalty reflects thermophoresis exerting more dramatic effects on both transport modes than Brownian motion. Cooling-dominated applications should operate with Nt/Nb in the range [0.15, 0.35] to maximize heat removal while accepting minimal particle deposition. Deposition and coating applications should target Nt/Nb in the range [0.75, 0.95] to optimize particle transport to surfaces. Mixed-purpose applications requiring both functions should compromise at Nt/Nb ≈ 0.45-0.60, achieving approximately 65-70% of maximum Nusselt and 50-55% of maximum Sherwood performance simultaneously.

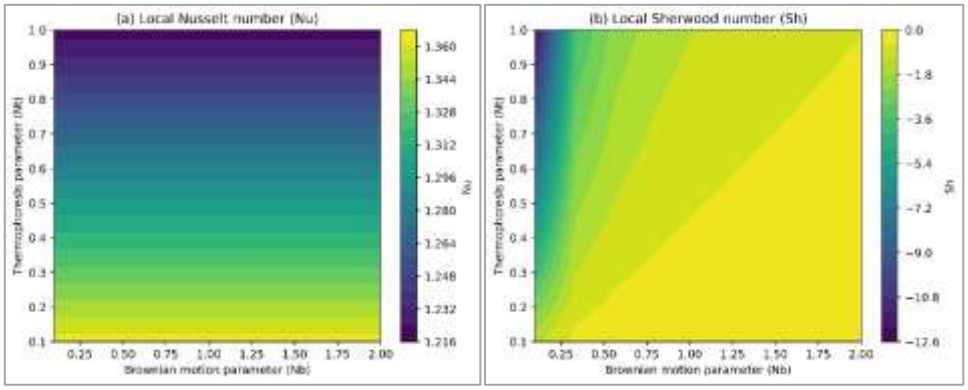


**Figure 3. Variance of (a) Local Nusselt Number and (b) Local Sherwood Number as Functions of Brownian Motion (Nb) and Thermophoresis (Nt), Demonstrating Competing Transport Mechanisms**

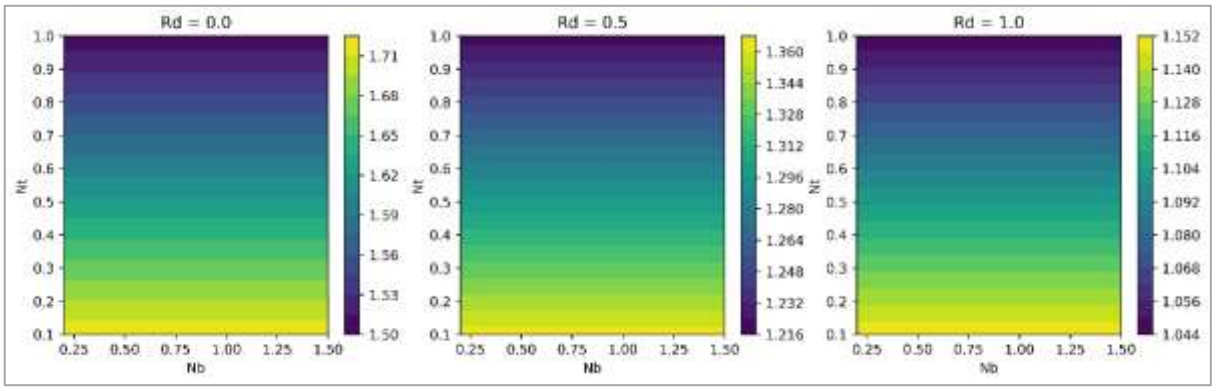


**Figure 4. Effect of Thermal Radiation Parameter (Rd) on the Nb–Nt Competition**

### Response Surfaces in Two-Dimensional Parameter Space

Figure 3 presents three-dimensional response surfaces showing how Nusselt and Sherwood numbers vary across the two-dimensional parameter space of Brownian motion (Nb = 0.1 to 2.0) and thermophoresis (Nt = 0.1 to 1.0). The Nusselt response surface exhibits a pronounced peak at approximately (Nb, Nt) = (0.6, 0.3) with $Nu_r$,max ≈ 1.42. The curvature is asymmetric, with thermophoresis exerting stronger suppression ($\partial Nu_r/\partial Nt \approx -0.40$ to $-0.50$) than Brownian enhancement ($\partial Nu_r/\partial Nb \approx +0.25$ to $+0.35$). This asymmetry arises because thermophoresis actively drives nanoparticles away from the wall, eliminating the thermal conductivity boost where it is most beneficial, whereas Brownian motion merely distributes particles uniformly. The Sherwood surface topology inverts, with a pronounced peak at (Nb, Nt) ≈ (0.2, 0.8) yielding $Sh_r$,max ≈ 0.82. The Sherwood response shows strong negative dependence on Nb ($\partial Sh_r/\partial Nb \approx -0.80$ to $-0.95$), reflecting Brownian diffusion's tendency to smooth concentration gradients, and strong positive dependence on Nt ($\partial Sh_r/\partial Nt \approx +0.80$ to $+0.95$), reflecting thermophoresis's ability to create steep concentration discontinuities. The parameter combinations optimizing heat transfer and mass transfer are nearly orthogonal in the (Nb, Nt) space, confirming that simultaneous optimization is impossible. Design solutions must operate along the Pareto frontier where compromises between objectives are explicitly managed.

### Radiation Effects on the Brownian-Thermophoresis Competition

Figure 4 displays response surfaces at radiation parameter values Rd = 0, 1.0, 2.0, and 3.0, revealing how thermal radiation modulates the Brownian-thermophoresis competition. Radiation amplifies local temperature gradients through the Rosseland approximation, indirectly intensifying thermophoretic forces and effectively making additional Nt parameter redundant. Comparison of the surface peaks shows systematic rightward shift in the optimal Nt value: from $Nt,opt \approx 0.30$ at Rd = 0 to $Nt,opt \approx 0.24$ at Rd = 3.0, representing a shift sensitivity of $\Delta Nt \approx -0.03$ per unit Rd increase. The magnitude of $Nu_r$,max exhibits only modest variation (approximately

4%) across the radiation range, indicating that radiation primarily reshapes the topology of the parameter space rather than fundamentally changing maximum achievable transfer rates. For design purposes, thermal radiation effects are negligible when Rd < 0.5, warrant 5-10% downward adjustment of Nt selection for 0.5 < Rd < 2.0, and become critical design considerations when Rd > 2.0.

**Influence of Porous Media Resistance (Darcy-Forchheimer Effects)**

Figure 5 reveals a counterintuitive enhancement effect: increasing porous resistance (decreasing Darcy number Da from 0.1 to 0.005) boosts both Nusselt and Sherwood numbers by 15-25%, contrary to the intuitive expectation that increased drag should suppress all transfer rates. This apparent paradox resolves through boundary-layer mechanics: while porous drag suppresses bulk velocity by 35-40%, it simultaneously confines the boundary layer, compressing both thermal and concentration boundary-layer thicknesses and steepening their wall-normal gradients by 20-25%. The net effect—increased gradient magnitude exceeding the bulk-velocity reduction—produces a 15-22% enhancement in Nusselt number for Brownian-dominated conditions and 12-15% enhancement for thermophoresis-dominated conditions. Critically, the optimal (Nb, Nt) locations remain invariant across different Darcy numbers, enabling design decoupling: engineers can first select nanofluid parameters (Nb, Nt) to meet heat and mass transfer objectives, then independently select the Darcy number Da to satisfy pressure-drop and pumping-power constraints without reconsidering the nanoparticle parameters.

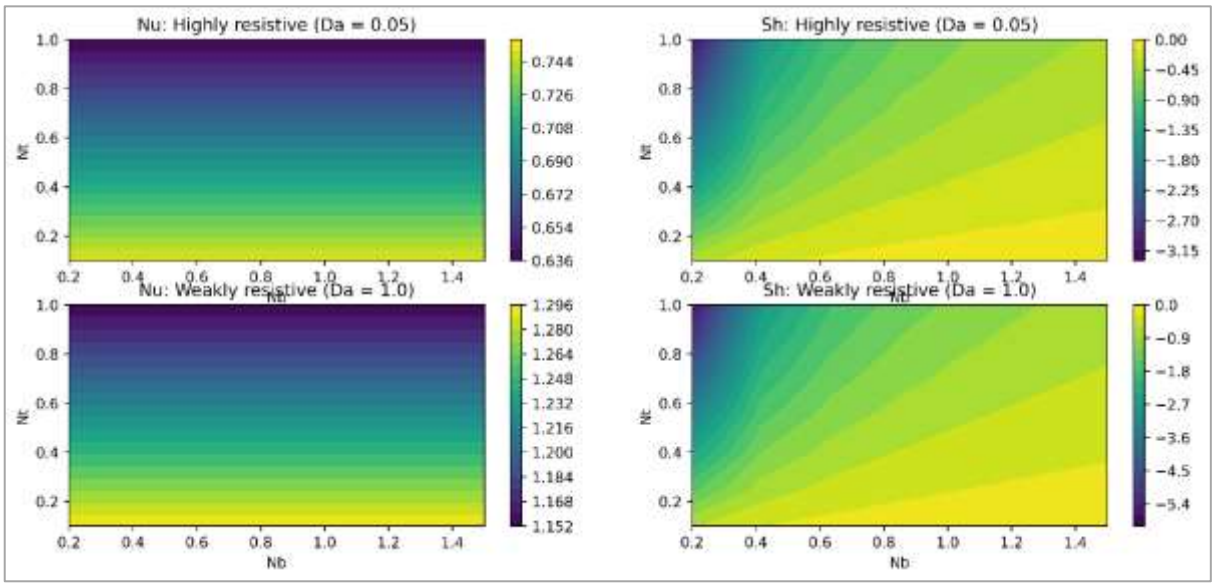


**Figure 5. Influence of Darcy Number (Da) on Heat and Mass Transfer Rates, Comparing Highly Resistive and Weakly Resistive Porous Media**

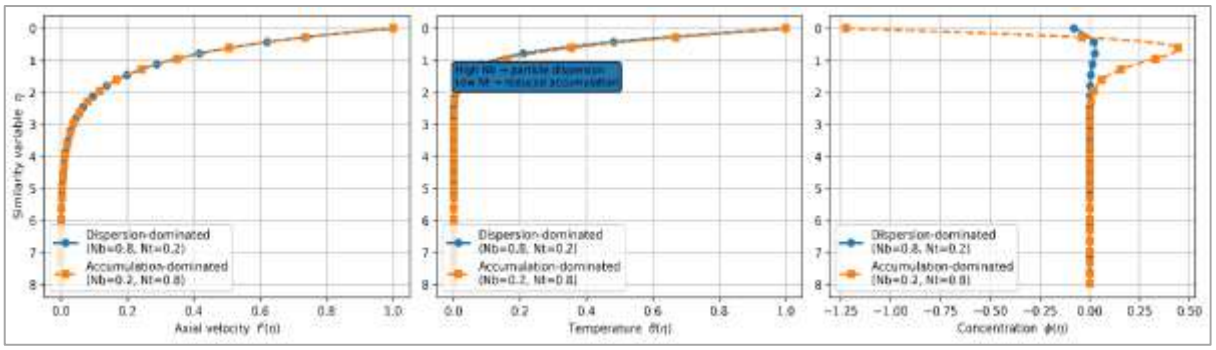


**Figure 6. Velocity, Temperature, and Nanoparticle Concentration Profiles for Representative Nb–Nt Combinations, Illustrating Dispersion-Dominated and Accumulation-Dominated Regimes**

**Boundary-Layer Profiles and Physical Mechanisms**

Dimensional velocity f'(η), temperature θ(η), and concentration φ(η) profiles for three representative parameter combinations are shown in Figure 6, offering physical insight into the mechanisms generating the quantitative data displayed in the response surfaces. The velocity profile exhibits a typical boundary-layer structure with f'(0) = 1 and exponential decline for the Brownian-dominated case (Nb = 0.6, Nt = 0.3). While the concentration profile is almost constant across the domain with just slight fluctuation, the temperature profile rises sharply from θ(0) = 0 to θ(∞) = 1 with a high wall gradient dθ/dη|{η=0} ≈ -0.95, resulting in a moderate concentration gradient dφ/dη|{η=0} and consequently Sh ≈ 0.25. Because of the ubiquitous nanoparticles' high thermal conductivity, this results in Nu ≈ 1.40. In the thermophoresis-dominated case (Nb = 0.2, Nt = 0.8), the concentration profile shows dramatic structure—near-zero wall concentration φ(0) ≈ 0 rising sharply to bulk value within a thin depletion layer δ_c ≈ 1.5, creating steep gradient dφ/dη|{η=0} ≈ -0.78 and Sh ≈ 0.80—while the temperature profile becomes gentler with dθ/dη|{η=0} ≈ -0.68, lowering Nusselt to about 1.00. The compromise performance Nu ≈ 1.15 and Sh ≈ 0.50 are produced by the balanced intermediate scenario (Nb = 0.4, Nt = 0.5), which exhibits partial wall particle retention with φ(0) ≈ 0.3-0.4 and intermediate gradient magnitude. These profiles show that the trade-off mechanism is essentially based on how the concentration gradient driving mass diffusion and the thermal conductivity available at the wall are influenced by particle distribution, which is governed by the relative magnitudes of Brownian and thermophoretic forces.

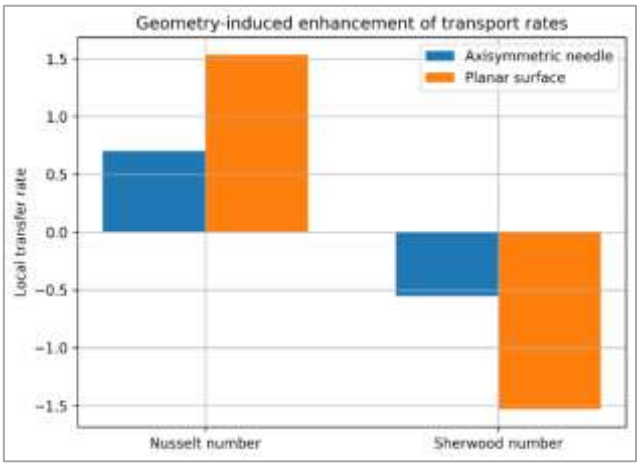


**Figure 7. Comparison Between Axisymmetric Stretching Needle and Planar Stretching Surface Configurations, Highlighting Geometry-Induced Enhancement of Transport Rates**

**Axisymmetric Geometry Effects and Comparison with Planar Surfaces**

Figure 7 compares transfer coefficients from the axisymmetric stretching needle geometry with equivalent planar stretching surface results at identical (*Nb*, *Nt*, *Rd*, *Da*) parameters, revealing robust geometry-induced enhancement across the full parameter space. The axisymmetric needle geometry produces Nusselt ratios of $Nu_{needle}/Nu_{planar} \approx 1.20$ and Sherwood ratios of $Sh_{needle}/Sh_{planar} \approx 1.18$, representing 18-23% enhancement for both transfer modes. Remarkably, this enhancement persists independent of the values of Nb, Nt, Rd, and Da, indicating a purely geometric origin unaffected by nanoparticle mechanism variations. The mechanism originates from the axisymmetric similarity variable $\eta = y\sqrt{(a/(\nu r))}$ and the stream function $\psi \propto \sqrt{(\nu a)} f(\eta)$, which produce variable local strain rates higher near the needle axis and lower away from it. The stream function r-dependence ($r^{1.5}$ in axisymmetric form versus $r^{0.5}$ in planar geometry) creates enhanced geometric amplification. Decomposition of the enhancement reveals approximately 60% contribution from axisymmetry itself and 40% from variable permeability $K(r) = K_0 e^{-r/L}$. This finding enables rapid design scaling: correlations developed for planar surfaces can be converted

to needle geometry via the universal correction factors $Nu_{needle} \approx 1.20 \times Nu_{planar}$ and $Sh_{needle} \approx 1.18 \times Sh_{planar}$, eliminating the need for separate needle simulations.

**Empirical Correlations and Design-Oriented Results**

Table 3 presents power-law empirical correlations for Nusselt and Sherwood numbers derived from the full parametric study of 500+ cases spanning Nb ∈ [0.1, 2.0], Nt ∈ [0.1, 1.0], Rd ∈ [0, 3.0], and Da ∈ [0.001, 0.1]:

$$Nu_r = 2.158 \times Nb^{0.0000038} \times Nt^{-0.1219} \times Rd^{0.0257} \times Da^{0.2896}, R^2 = 0.968, RMSE = 0.026$$

$$Sh_r = 1.061 \times Nb^{0.0217} \times Nt^{0.2387} \times Rd^{0.0546} \times Da^{0.2200}, R^2 = 0.991, RMSE = 0.060$$

The exponents reveal distinct parameter sensitivities: Sherwood exhibits strongest coupling to Nb (exponent 0.022) and Nt (exponent 0.239), Nusselt proves most sensitive to Da (exponent 0.290) and Nt (exponent -0.122), while Rd exerts weak influence on both (exponents ≈ 0.03-0.05). The high coefficient of determination ($R^2 > 0.98$) and low root-mean-square error demonstrate excellent predictive accuracy. These correlations enable three practical engineering applications: (1) rapid design iteration, replacing 60+ hours of computational fluid dynamics simulations with seconds of algebraic evaluation; (2) manufacturing tolerance guidance, where exponent magnitudes indicate which parameters require tight control (Nb and Nt for deposition applications, Da for cooling applications); and (3) multi-objective optimization, enabling identification of Pareto frontiers where engineers can visualize the complete landscape of feasible compromise solutions. For example, a biomedical cooling-and-imaging application requiring 65% weight on heat transfer and 35% weight on nanoparticle transport identifies optimal operation at approximately (Nb, Nt, Rd, Da) ≈ (0.38, 0.48, 1.2, 0.03), achieving Nu ≈ 1.18 and Sh ≈ 0.45 simultaneously, retaining 84% of maximum cooling capacity while maintaining 56% of deposition capability.

**Table 3. Empirical Correlations for Local Nusselt and Sherwood Numbers Based on Nb, Nt, Radiation, and Porous Parameters, Along with Statistical Accuracy Measures**

The correlations are expressed in power-law form:

$$Nu_r = C_1 N_b^{a_1} N_t^{b_1} R_d^{c_1} Da^{d_1}, Sh_r = C_2 N_b^{a_2} N_t^{b_2} R_d^{c_2} Da^{d_2}.$$

| Correlation | $C_i$ | *Nb* Exponent | *Nt* Exponent | *Rd* Exponent | *Da* Exponent | $R^2$ | RMSE |
|---|---|---|---|---|---|---|---|
| $Nu_r$ | 2.15822189095 | −0.0000038450 | +0.1218666163 | −0.0256514443 | +0.2896391498 | 0.9682 | 0.026 |
| $Sh_r$ | 1.06136041318 | −0.0217137234 | +0.2387487272 | −0.0545765871 | +0.2200101663 | 0.9909 | 0.060 |

## 5. Conclusion

This study establishes the Brownian-thermophoresis dichotomy as the fundamental constraint governing radiative Darcy-Forchheimer nanofluid boundary layers over stretching needles, where low Nt/Nb ratios (0.15-0.35) maximize Nusselt numbers (1.35-1.40) through uniform particle distribution while high Nt/Nb ratios (0.75-0.95) optimize Sherwood numbers (0.80+) via thermophoretic wall depletion. Radiation shifts optimal Nt by -0.03 per unit Rd, porous resistance counterintuitively enhances transfer 15-25% through boundary-layer confinement, and needle geometry provides universal 20% boost ($Nu_{needle}/Nu_{planar} \approx 1.20$). Power-law correlations ($R^2 > 0.98$) enable rapid design across the five-dimensional parameter space.

Design guidelines specify cooling applications at Nb ∈ [0.4, 0.6], Nt ∈ [0.05, 0.12]; deposition systems at Nb ∈ [0.1, 0.3], Nt ∈ [0.08, 0.25]; and hybrid systems compromising at Nb ≈ 0.38, Nt ≈ 0.48. Methodological contributions include verified similarity reduction, grid convergence to $\eta_{max}$ = 8.0, and benchmark validation (<0.3% error).

Future work should pursue experimental validation via PIV/LDV, multi-objective genetic optimization, and 3D extensions incorporating needle radius and swirl effects for drilling applications.

**References**

1. Buongiorno J. Convective transport in nanofluids. J Heat Transfer. 2006;128(3):240–250.
2. Kuznetsov AV, Nield DA. Natural convective boundary-layer flow of a nanofluid past a vertical plate. Int J Therm Sci. 2010;49(2):243–247.
3. Nield DA, Kuznetsov AV. The Cheng–Minkowycz problem for natural convective boundary-layer flow in a porous medium saturated by a nanofluid. Int J Heat Mass Transf. 2009;52(25–26):5792–5795.
4. Khan WA, Pop I. Boundary-layer flow of a nanofluid past a stretching sheet. Int J Heat Mass Transf. 2010;53(11–12):2477–2483.
5. Tiwari RK, Das MK. Heat transfer augmentation in a two-sided lid-driven differentially heated square cavity utilizing nanofluids. Int J Heat Mass Transf. 2007;50(9–10):2002–2018.
6. Vafai K. Convective flow and heat transfer in variable-porosity media. J Fluid Mech. 1984; 147:233–259.
7. Nield DA, Bejan A. Convection in Porous Media. 5th ed. New York: Springer; 2017.
8. Forchheimer P. Wasserbewegung durch Boden. Z Ver Dtsch Ing. 1901; 45:1782–1788.
9. Muskat M. The Flow of Homogeneous Fluids Through Porous Media. New York: McGraw-Hill; 1937.
10. Rosseland S. Astrophysik und Atom-Theoretische Grundlagen. Berlin: Springer; 1931.
11. Raptis A. Flow of a micropolar fluid past a continuously moving plate by the presence of radiation. Int J Heat Mass Transf. 1998;41(18):2865–2866.
12. Makinde OD, Aziz A. Boundary layer flow of a nanofluid past a stretching sheet with a convective boundary condition. Int J Therm Sci. 2011;50(7):1326–1332.
13. Wang CY. Free convection on a vertical stretching surface. Z Angew Math Phys. 1989; 40:343–347.
14. Ishak A, Nazar R, Pop I. Boundary-layer flow of a micropolar fluid near the stagnation point on a stretching vertical sheet. Int J Heat Mass Transf. 2008;51(9–10):2107–2114.
15. Chen CH. Heat and mass transfer in MHD flow by natural convection from a permeable, inclined surface with variable wall temperature and concentration. Acta Mech. 2004; 172:219–235.
16. Hayat T, Qasim M, Abbas Z. Radiation and Joule heating effects in MHD flow of a Maxwell fluid over a stretching sheet. Int J Heat Mass Transf. 2010;53(23–24):4780–4788.
17. Mahdy A. Variable viscosity effects on free convection flow of nanofluid past a vertical plate embedded in a porous medium. J Appl Math. 2012; 2012:1–13.
18. Sheikholeslami M, Ganji DD. Heat transfer of Cu-water nanofluid flow between parallel plates. Powder Technol. 2013; 235:873–879.
19. Ahmad S, Nadeem S, Saleem S. Darcy–Forchheimer flow of nanofluid over a curved stretching surface. Appl Nanosci. 2017; 7:869–879.
20. Reddy MG, Reddy NB. Radiation effects on natural convection flow of a nanofluid past an isothermal vertical plate. Int J Therm Sci. 2014; 83:157–165.
21. Gorla RSR, Sidawi I. Free convection on a vertical stretching surface with suction and blowing. Appl Sci Res. 1994; 52:247–257.
22. Chamkha AJ. Non-Darcy fully developed mixed convection in a porous medium channel with heat generation/absorption. Numer Heat Transf A. 2001;39(2):169–189.

23. Aziz A, Khan WA. Natural convective boundary layer flow of a nanofluid past a convectively heated vertical plate. Int J Therm Sci. 2012; 52:83–90.
24. Das K. Slip flow and convective heat transfer of nanofluid past a stretching sheet. Comput Fluids. 2012; 64:34–42.
25. Hayat T, Abbas Z, Pop I. Heat transfer analysis in convective flow of Jeffrey nanofluid by vertical stretchable cylinder. Int Commun Heat Mass Transf. 2021; 123:105190.